Computational Investigation of Regimes of the Arc in Crossflow

V. G. Bhigamudre[1] and J. P. Trelles[1]

[1] *Department of Mechanical Engineering, University of Massachusetts Lowell, 1 University Ave, Lowell, MA 01854, USA*

Abstract: The arc in crossflow, a canonical plasma configuration found in industrial applications such as wire-arc spraying and circuit breakers involves perpendicular gas impingement onto an electric arc. A two-temperature computational fluid dynamics model is used to investigate the coupled fluid-thermal-electromagnetic phenomena involved in the crossflow arc-plasma interaction. Simulation results shown that this interaction leads to distinct flow regimes, from steady to periodic, quasi-periodic, and potentially, to turbulent.

Keywords: thermal plasma, two-temperature model, dimensional analysis, flow regimes.

1. Introduction

Wire arc spraying is a robust materials deposition technique used in applications such as corrosion and oxidation prevention, and medical implants. Low-voltage circuit breakers are used in industrial machinery, battery systems, etc. Both types of industrial applications involve the perpendicular impingement of a working gas stream onto an arc, a configuration commonly referred to as the arc in crossflow [1-5]. Figure 1 shows schematics of the wire arc spraying process and a low-voltage circuit breaker. The wire arc spraying system consists of continuously fed of metallic wires as electrodes forming a plasma arc that interacts with a stream of impinging gas flow. The plasma melts the electrodes, while the gas flow drags the molten metal particles which are deposited to a substrate. In low-voltage circuit breakers, a high voltage leak in the system is prevented by initiating a mechanism that separates the electrodes leading to ionization within the gap, ultimately forming an electric arc. This arc must be extinguished with a metallic splitter and a cold-gas flow. Both applications are based on a similar plasma flow configuration, i.e., the so-called arc in crossflow.

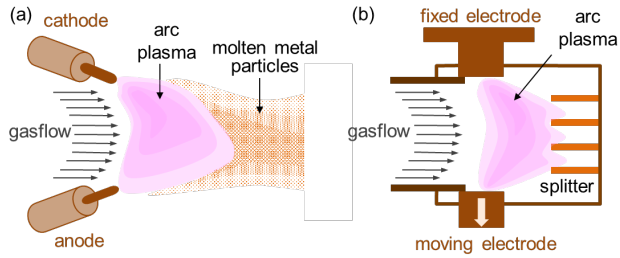

Fig. 1. Industrial applications based on an arc in crossflow: (a) wire arc spraying and (b) low-voltage circuit breaker.

Figure 2 shows the schematics of a canonical arc in crossflow. A direct-current (dc) cathode and an anode are enclosed within confining parallel walls separated by a distance H. An imposed electric field causes arc formation driven by a total amount of electric current I_{tot}. The plasma is impinged perpendicularly by a gas stream with mean axial velocity U_i at the inlet, causing convective cooling and drag, forcing the plasma to bend and produce an afterglow downstream. The main operating parameters for the arc in crossflow are the type of gas, the inter-electrode spacing H, the total current I_{tot}, and the inflow velocity U_i.

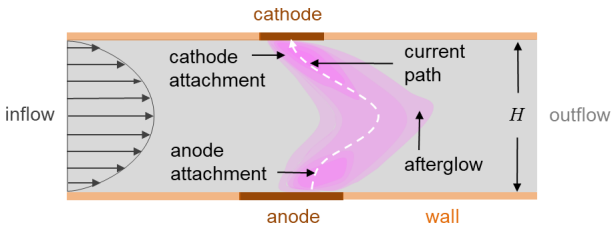

Fig. 2. Schematic of an arc in crossflow system: showing the plasma attachment to the electrodes with inter-electrode distance H, the attachments, the current path, and the nonequilibrium afterglow plasma.

The arc in crossflow has been extensively studied experimentally [1], theoretically [3], and computationally [2]. All previous investigations of the arc in crossflow have relied on models based on the assumption of Local Thermodynamic Equilibrium (LTE) between the heavy-species and the electrons. This assumption is valid in the plasma core but is not applicable to the gas-plasma interaction region or plasma periphery [6]. A non-LTE (NLTE) model can provide fundamental insight of the arc in crossflow, particularly of the plasma-gas interaction regions, where thermodynamics nonequilibrium is expected to be predominant. A computational fluid dynamics NLTE model is used to investigate the coupled fluid-thermal-electromagnetic phenomena involved in the crossflow arc-plasma interaction, which is shown to lead to distinct flow regimes.

2. Mathematical model

The plasma is considered to be quasi-neutral, non-magnetized, non-relativistic, optically thin, compressible, reactive, electromagnetic fluid in chemical equilibrium

and thermodynamic nonequilibrium (NLTE). Charge transport is dominated by the electric field distribution and electron diffusion. Ion diffusion, Hall currents, and electrode sheaths are neglected.

The set of equations describing the NLTE plasma flow are constituted by: mass conservation, mass-average momentum conservation, conservation of thermal energy of heavy-species and of electrons, electric charge and magnetic induction conservation. These equations form a single set of coupled transient-advective-diffusive-reactive (TADR) transport equations listed in **Table 1**.

Table 1: Set of fluid-electromagnetic evolution equations for the NLTE plasma flow model. For each equation: Transient + Advective – Diffusive − Reactive = 0.

Equation	Transient	Advective	Diffusive	Reactive
Conservation of total mass	$\partial_t \rho$	$\mathbf{u}\cdot\nabla\rho + \rho\nabla\cdot\mathbf{u}$	0	0
Conservation of linear momentum	$\rho\partial_t \mathbf{u}$	$\rho\mathbf{u}\cdot\nabla\mathbf{u} + \nabla p$	$\nabla\cdot\boldsymbol{\tau}$	$\mathbf{J}_q \times \mathbf{B}$
Thermal energy (heavy-species)	$\rho\partial_t h_h$	$\rho\mathbf{u}\cdot\nabla h_h$	$\nabla\cdot(\kappa_{hr}\nabla T_h)$	$D_t p_h + K_{eh}(T_e - T_h) - \boldsymbol{\tau}:\nabla\mathbf{u}$
Thermal energy (electrons)	$\rho\partial_t h_e$	$\rho\mathbf{u}\cdot\nabla h_e$	$\nabla\cdot(\kappa_e\nabla T_e)$	$D_t p_e - K_{eh}(T_e - T_h) - 4\pi\varepsilon_r$ $+\mathbf{J}_q\cdot(\mathbf{E} + \mathbf{u}\times\mathbf{B}) + \frac{5k_B}{2e}\mathbf{J}_q\cdot\nabla T_e$
Charge conservation	0	0	$-\nabla\cdot\mathbf{J}_q$	0
Magnetic induction	$\partial_t \mathbf{A}$	$\nabla\phi_p - \mathbf{u}\times(\nabla\times\mathbf{A})$	$\left(\frac{1}{\mu_0\sigma}\right)\nabla^2\mathbf{A}$	$\mathbf{0}$

In table 1, $\partial_t = \partial / \partial t$ represents the partial derivative with respect to time, ∇ and $\nabla\cdot$ represent the gradient and divergence operators, respectively; ρ is mass density, p pressure, $\mathbf{u}$ mass-averaged velocity, μ dynamic viscosity, $^{\mathsf{T}}$ the transpose operator, and $\boldsymbol{\delta}$ the Kronecker delta tensor; $\mathbf{J}_q$ is the electric current density and $\mathbf{B}$ is the self-induced magnetic field; $\mathbf{E}$ is the real electric field; h_h and h_e are enthalpies of heavy-species and electrons, respectively, κ_{hr} is the translational-reactive heavy-species thermal conductivity, κ_e is the translational thermal conductivity of electrons; $D_t p_h$ and $D_t p_e$ represents pressure work by the heavy-species and electrons, respectively; K_{eh} is the energy exchange coefficient between electron and heavy-species, $\boldsymbol{\tau}$ represents the stress tensor for a Newtonian fluid, ε_r is effective net radiative energy emission coefficient; $\mathbf{A}$ the magnetic vector potential. A more detailed description of the model and the nomenclature used are described in [7].

The set of equations in **Table 1** are solved for the variables: pressure p, velocity components u_x, u_y, u_z, heavy-species temperature T_h, electron temperature T_e, electric potential ϕ_p, and magnetic vector potential $\mathbf{A}$.

To solve for the unknown variables, the Variation Multiscale Finite Element Method (VMS-FEM) has been used. This method has proven effective for the modeling and simulation of plasma flow which typically complex multi-scale and non-linear characteristics [7]. A detailed description of the computational geometry and the boundary conditions for the arc in crossflow implemented in this research is found in [4].

3. Results

Representative 3D steady-state solution fields, corresponding to operating conditions: I_{tot} = 34 [A] and U_{imax} = 0.5 [ms^{-1}], are presented in the figure 3.

Pressure increases near the electrodes due to the electromagnetic pinching (Maecker effect) caused by concentrated current density, especially along the cathode surface. This lead to the formation of a cathode jet, which can be observed in figure 3(b). The arc shape of the arc, as given by the heavy-species T_h and the electron T_e temperature distributions, is mainly a result of the imbalance between the self-induced electromagnetic force and the gas drag force due to impinging of the cold gas on the hot arc. The deviation from thermal equilibrium is clearly noticeable between figures 3(c) and 3(d), which showcase the constricted distribution of T_h and the relatively more diffuse distribution of T_e. The degree of deviation from LTE is discussed in greater detail in [4]. The electric potential ϕ_p distribution, as seen in figure 3(e), shows a somewhat abrupt change. The distribution of magnetic potential reflects the shape of the arc.

The set of parameters controlling the arc in crossflow are the total current I_{tot}, the maximum inflow velocity U_{imax}, the inter-electrode spacing H, and the gas type. These can be analyzed more effectively through non-dimensional numbers. A sufficient set of non-dimensional

numbers to characterize the arc in crossflow are: the Reynolds number *Re* and the Enthalpy number Π_h [4]. The Reynolds number is an estimate of the ratio of the magnitude of advective transport to that for the diffusive transport, while the Enthalpy number is an estimate of the ratio of the magnitude of the thermal energy transported by the flow to the electrical energy input. The dimensionless numbers *Re* and Π_h are given by [8]:

$$Re = \frac{\rho_i U_{i\max} H}{\mu_i} \quad \text{and} \quad \Pi_h = \frac{\sigma_r h_r \rho_r U_{i\max} H^3}{I_{tot}^2}, \qquad (1)$$

where the subscripts '*r*' denotes the value of a given property evaluated at reference conditions (temperature equal to 16.7 kK in the present work) and '*i*' denotes values evaluated at the inlet conditions.

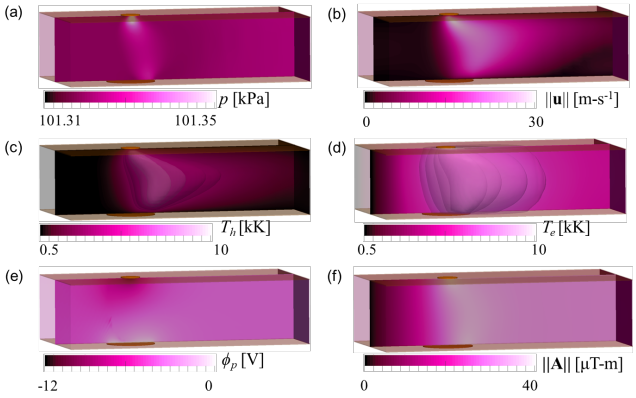

Fig. 3. Steady-state solution fields of: (a) pressure, (b) velocity magnitude, (c) heavy-species temperature, (d) electron temperature, (e) electric potential and (f) magnetic vector potential for conditions: argonm, I_{tot} = 34 [A] and U_{imax} = 0.5 [ms^{-1}].

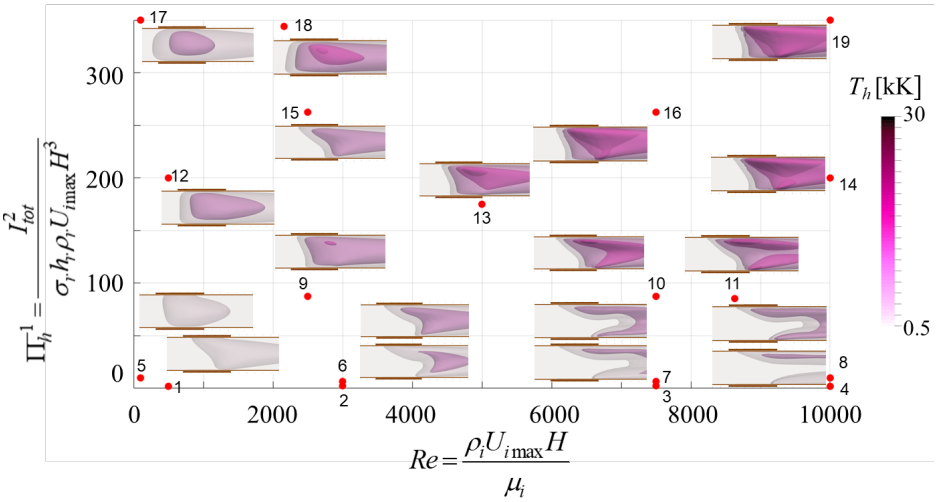

Fig. 4. Characterization of the arc in crossflow: iso-surfaces of T_h = 2, 8, 15, 20 [kK] as a function of the Reynolds number *Re* and the inverse Enthalpy number Π_h^{-1}.

The arc in crossflow is characterized by a set of 19 computational simulations. Representative results of the characterization are shown in figure 4 given by the iso-surfaces of T_h at 2, 8, 15, 20 [kK] as function of *Re*-Π_h^{-1} in the range $0 < Re < 10^4$ and $2 < \Pi_h^{-1} < 350$. The results show that the arc shape changes from cusp-shaped to bow-shaped with increasing *Re* or for a reduction in Π_h^{-1}. The curvature and deflection of the arc are largest for the maximum *Re* and minimum Π_h^{-1} studied (case 4). The heavy-species temperature T_h increases with increasing *Re* and Π_h^{-1} as a result of stronger gas cooling leading to greater arc constriction.

The results in figure 4 depict the intricate interplay between *Re* and Π_h on determining the characteristics of the arc in crossflow. The simulations of the 19 cases have also shown that the arc fluctuates about an equilibrium position with time. These fluctuations in the arc in crossflow somewhat resemble those found in more complex plasma configurations, such as non-transferred arc plasma torches [9, 10]. The complex dynamics of the arc in crossflow are the result of the coupled fluid dynamic-thermal-electromagnetic phenomena caused by the arc-gas flow interaction. These dynamics manifest as distinct flow regimes, such as steady, periodic, quasi-periodic, and potentially to even turbulent [11].

Figure 5 shows simulation results representative of the fluctuations of the arc, which are captured at four representative locations, as indicated in figure 5(a), i.e. Near-cathode, Upstream, Midstream, and Downstream. The locations are chosen to provide a somewhat clear depiction of the arc dynamics and to be representative of experimental diagnostic efforts. The effect of increasing *Re* (assuming Π_h approximately constant) is shown in figures 6 (c-f), where the left frame shows the arc shape, and the right shows the arc voltage fluctuations $\delta\phi_p$ with respect to the mean voltage drop i.e., $\delta\phi_p = \phi_p - \phi_{p,mean}$.

From the results in figure 5(b-e), it can be observed that despite a constant current imposed at the cathode and a constant inflow, the arc voltage fluctuates with time, indicating the existence of a persistent balance between flow energy and electrical energy. The amplitude of the fluctuations of the electric potential $\delta\phi_p$ decreases with increasing Reynolds number. Additionally, for low Reynolds numbers, there is a phase delay of the voltage fluctuations that decreases for increasing *Re*. Additionally, the for highest *Re* simulations, the voltage fluctuations are heavily-convoluted. These fluctuations suggest the existence of an underlying energy exchange mechanism and indicate the existence of various flow regimes such as steady, periodic, quasi-periodic, chaotic, and potentially turbulent.

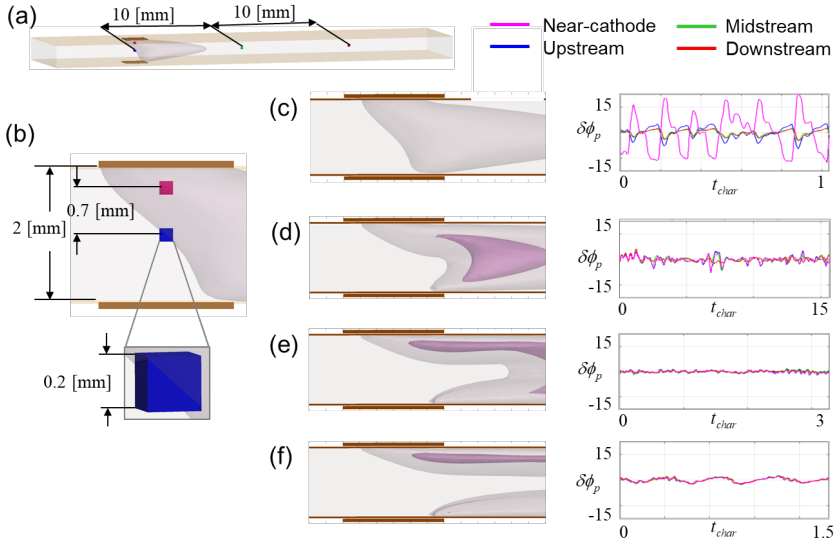

Fig. 5. Dynamics of the arc in crossflow: (a) Locations of the dynamic measurements, (b) dimensions of the probing boxes; and results for simulation sets (Re, Π_h^{-1}): (b) (500, 2), (c) (3000, 2.5), (d) (7500, 2.5), and (e) (10000, 2); (*left*) iso-surfaces of 2 and 8 (kK), and (*right*) temporal fluctuations of the arc voltage.

4. Conclusion

The arc in crossflow is a plasma configuration commonly encountered in industrial applications such as circuit breakers and wire arc spraying. A 3D time-dependent NLTE plasma flow model is used to computationally characterize a canonical arc in crossflow. The modeling results show that thermal nonequilibrium is dominant in the plasma-gas interaction and plasma-electrode regions. The characterization of the arc in crossflow based on the Reynolds and the Enthalpy numbers revealed, which provide a minimal yet complete set of controlling parameters. Simulation results showed that the gas-plasma flow interaction, involving coupled fluid dynamic-thermal-electromagnetic phenomena, leads to distinct flow regimes, from steady to periodic, quasi-periodic, and potentially, to turbulent.

Acknowledgments

The authors gratefully acknowledge support from the US National Science Foundation, Division of Physics, through award number PHY-1301935.

References

[1] D. M. Benenson, A. J. Baker, and A. A. Cenkner, IEEE Transactions on Power Apparatus and Systems, **88**, 5, (1969).

[2] M. Kelkar and J. Heberlein, J. Phys. D: Appl. Phys. , **33**, (2000).

[3] H. H. Maeckar and H. G. Stablein, IEEE Transactions on Plasma Science, **14**, 4, (1986).

[4] V. G. Bhigamudre and J. P. Trelles, Journal of Physics D: Applied Physics, **52**, 1, (2019).

[5] V. G. Bhigamudre and J. P. Trelles, in 2017 IEEE International Conference on Plasma Science (ICOPS), (2017).

[6] J. P. Trelles, Journal of Physics D: Applied Physics, **40**, (2007).

[7] J. P. Trelles and S. M. Modirkhazeni, Comput. Methods Appl. Mech. Engrg., **282**, (2014).

[8] O. I. Yas'ko, Pure and Appl. Chem, **62**, 9, (1990).

[9] W. Pan, X. Meng, and C. Wu, Plasma Science and Technology, **8**, 4, (2006).

[10] R. Huang, H. Fukanuma, Y. Uesugi, and Y. Tanaka, Journal of Thermal Spray Technology, **21**, 3-4, (2011).

[11] L. Niemeyer and K. Ragaller, Z. Naturforsch, **28a**, (1973).